Luminescence nanothermometry using self-assembled Er^{3+}, Yb^{3+} doped Y_2O_3 nanodiscs: might the upconversion mechanism condition their use as primary thermometers?

Albenc Nexha, Maria Cinta Pujol,* Francesc Díaz, Magdalena Aguiló, and Joan J. Carvajal*

Universitat Rovira i Virgili, Departament Química Física i Inorgànica, Física i Cristal·lografia de Materials i Nanomaterials (FiCMA-FiCNA), Campus Sescelades, E-43007, Tarragona, Spain

*mariacinta.pujol@urv.cat

*joanjosep.carvajal@urv.cat

Abstract

Self-assembled Er^{3+}, Yb^{3+} doped Y_2O_3 colloidal nanodiscs were synthesized *via* a digestive ripening process using oleic acid and oleylamine as organic surfactants, and NaCl as the structure-directing agent. X-ray powder diffraction confirms the formation of cubic yttrium oxide, regardless of the doping concentration, although this affects to the crystallinity of the samples. Transmission electron microscopy (TEM) and high-resolution transimission electron microscopy (HRTEM) images reveal that these nanodiscs tend to self-assemble in fiber-like structures on the grids, with an average diameter of 20 nm, thicknesses down to the unit cell, and lengths of several micrometers. The Er^{3+}, Yb^{3+} doped Y_2O_3 nanodiscs were tested as luminescent nanothermometers operating in the visible region. Upon excitation at 980 nm, three emission bands were generated at 525 nm, 550 nm, and 650-690 nm, assigned to $^2H_{11/2}\rightarrow{}^4I_{15/2}$, $^4S_{3/2}\rightarrow{}^4I_{15/2}$ and $^4F_{9/2}\rightarrow{}^4I_{15/2}$ electronic transitions of Er^{3+} ions, respectively. A relative thermal sensitivity of 1.11% K^{-1} and a temperature uncertainty of 0.44 K at room temperature were determined for these thermometers. However, the possibility of using them as primary luminescent thermometers was ruled out by the important amount of heat released by the four-photons upconversion mechanism for the generation of the green light in the 4 mol% Er^{3+} and 4 mol% Yb^{3+} doped Y_2O_3 nanodiscs.

I. Introduction

The development of the so-called non-contact nanothermometers as potential replacement of the traditional contact thermometers for temperature sensing applications, has provided temperature knowledge at the submicron level, previously unreachable from the traditional contact thermometers.[1] These temperature readings at the submicron level are crucial for the optimization of photothermal cancer therapies,[2] and for the investigation of cellular processes like enzyme reactions or metabolism.[3] Non-contact luminescent thermometers are optically-based and rely on the variation of the emission of luminescent material as the temperature changes. Temperature-dependent parameters of luminescence involve intensity, lifetime, bandwidth, band shape, spectral position and polarization.[1] Several types of luminescent thermometers have been developed through the years such as polymers,[4] DNA and protein conjugated systems,[5] organic dyes,[6] quantum dots,[7] transition metal containing compounds,[8] and lanthanide doped materials.[1]

Lanthanide doped materials have attracted great interest attributed to their peculiar electronic configuration, which allows for narrow emission bands, long emission lifetimes (in the range of microseconds to milliseconds), good chemical and physical stability, and low toxicity.[1] In addition, lanthanide doped luminescent nanothermometers present the ability to convert low-energy near-infrared (NIR) photons into higher-energy ultraviolet (UV) or visible (VIS) photons.[9, 10] This allows overcoming problems related with the autofluorescence arising from the biological tissues and damaging of the surrounding healthy tissues in biological applications when excited with UV or VIS light sources.[11, 12] The materials that exhibit these conversion abilities are called upconverting luminescent materials. The unique anti-Stokes properties of these particles have led to the development of a plethora of applications, spanning from thermal sensing and light-triggered drug delivery to solar energy harvesting and super-resolution microscopy.[9, 13] Due to these potential applications, the synthesis and the spectroscopy of the upconverting nanoparticles has attracted a great interest among the scientific community.

The luminescence of the lanthanide upconverting nanoparticles and their corresponding thermometric performance are strongly temperature dependent. Hence, the generated luminescence and the thermometric properties of a lanthanide doped material are highly influenced by several factors. The temperature interval in which the particles are analyzed or the synthetic methodology applied to synthesize these particles, which generates different sizes and shapes, highly tune the temperature sensing properties of the material.[1, 14,

15] Other factors such as the surface quenching mechanisms directly related to the organic surfactants bounded to the surface of the final product, and the chosen dopants, either in the role of the activator or the sensitizer, as well as the selection of the host material, have high impact of the temperature sensing properties.[14] Finally, exciting the upconversion (UC) phenomena in these luminescent nanoparticles through anti-Stokes mechanisms, also affects their thermometric performance.[16] For example, the change of crystallographic structure in Er^{3+} doped ZnO nanocrystals, upon annealing, from a cubic into a hexagonal crystalline phase, generated not only brighter photoluminescence but also a better thermometric performance due to the change of the energy gap between the two excited levels (a wider energy gap led to higher thermal sensitivity).[17] The size of the particles may also influence their thermometric performance[10, 15]. Generally, if we compare the performance of a micrometer-sized material with the same component but nanosized, the temperature dependence of the luminescence becomes more dominant at the latter, assigned to the increasing role of the surface defects and the increase of the surface-to-volume ratio.[15] On the other hand, the quenching effect that surface defects or other ligands attached to the surface can generate, results in a reduced brightness of the photoluminescence and the consequent reduced quantum yield of the upconverting nanocrystals.[18]

Erbium (Er^{3+}) ion constitutes an excellent candidate for UC luminescence as its electronic states can be populated with low cost NIR energy sources.[19, 20] In addition, the energy gap between these electronic states is in the range of 700 cm^{-1}, being an ideal ion for its use in Boltzmann based thermometry within the physiological range of temperatures.[21] Using ytterbium (Yb^{3+}) ion as sensitizer can boost the luminescence intensity of the Er^{3+} activator in upconverting materials due to the large absorption cross-section at 980 nm and efficient energy transfer towards Er^{3+} that Yb^{3+} has.[22, 23] The choice of host strongly determinates the temperature sensing applications (among others) of these upconverting materials.[24-26] Among different host materials for Er^{3+}/Yb^{3+} ions, yttrium oxide (Y_2O_3) is viewed as an attractive choice due to several properties, including low phonon energy (in the range of 550-590 cm^{-1}, comparable to that of oxysulfides (520 cm^{-1})), and slightly higher than fluorides (400-500 cm^{-1})),[27] chemical inertness, large band gap energy (typically around 5.8 eV), high melting point (~2698 K), high dielectric constant (around 13-18),[28] and low toxicity.[29] Due to these, Y_2O_3 has been extensive explored as a luminescent material for biological labeling, optoelectronics, and scintillator luminescence devices.[30, 31] Due to size match with the lanthanide series,[32] the luminescence generated by Y_2O_3 materials doped with these ions, has interest in the development of fluorescent lamps, LEDs and displays, and *in vivo* biological imaging.[31] These applications are highly dependent on the size, shape and crystalline phase of this host. As a typical example, red emitting Eu^{3+} doped Y_2O_3 particles have demonstrated to enhance the photoluminescence intensity in the shape of 2D plates *versus* dots, and in addition, the intensity of the fluorescence of the cubic Y_2O_3 phase is significantly higher when compared to that of its monoclinic phase.[33, 34]

Different synthetic routes provide different shapes of Y_2O_3 particles, such as nanodiscs,[35] nanoplates,[36] wires,[37] or flower-like structures,[38] and even different crystallographic structures. Flame spray pyrolysis,[39] combustion,[40] and precipitation/sol-gel methods,[41] produced cubic Y_2O_3, while gas-phase condensation,[42] and laser deposition,[43] produce monoclinic Y_2O_3. Finally, non-hydrolytic procedures ([44], [35], [36]) produce cubic distorted or low crystallinity structures.

Here, we investigate the ability to produce self-assembled Er^{3+},Yb^{3+} doped cubic Y_2O_3 colloidal nanodiscs with thicknesses down to a unit cell to act as luminescent nanothermometers in the visible operating in the 298-338 K range of temperatures, after excitation with a NIR 980 nm laser source. Their temperature sensing properties are determined by the intensity ratio of thermally coupled energy levels, which generate the green emissions located at 525 nm and 550 nm, arising from Er^{3+}. Based on these green emissions, we explored the probability of using these nanodiscs as primary thermometers, *i.e.* materials whose performance as thermometers is predicted by well-known state equations, with all parameters or constants determined *a priori*, without requiring any previous calibration, so that they can be applied as a reference or standard thermal readout.[45]

II. Experimental section

2.1. Materials

Yttrium acetate hydrate ($Y(CH_3CO_2)_3 \cdot H_2O$ as $Y(Ac)_3 \cdot H_2O$, 99.99%), erbium acetate tetrahydrate ($Er(CH_3CO_2)_3 \cdot 4H_2O$ as $Er(Ac)_3 \cdot 4H_2O$, 99.99%) and oleylamine (OLAM, >70%) were purchased from Sigma Aldrich. Ytterbium acetate tetrahydrate ($Yb(CH_3CO_2)_3 \cdot 4H_2O$ as $Yb(Ac)_3 \cdot 4H_2O$, 99.99%) was purchased from

Apollo Scientific. Oleic acid (OLAC, 90%) and n-hexane (99%) were purchased from Alfa Aesar. Sodium chloride (NaCl) and ethanol (EtOH) were purchased from Merck and VWR, respectively. All chemicals were used without further purification.

2.2. Synthesis of self-assembled yttrium oxide colloidal nanodiscs

Self-assembled Y_2O_3 colloidal nanodiscs doped with 4 mol% Er^{3+}, 4 mol% Yb^{3+} and 10 mol% Er^{3+}, 10 mol% Yb^{3+}, were synthesized using a digestive ripening synthetic protocol.[46]

In a typical digestive ripening-based synthesis of 4 mol% Er^{3+} and 4 mol% Yb^{3+} doped Y_2O_3 nanocrystals, 0.184 mmol of $Y(Ac)_3{\cdot}H_2O$, 0.008 mmol of $Er(Ac)_3{\cdot}4H_2O$, 0.008 mmol of $Yb(Ac)_3{\cdot}4H_2O$, and 0.1 mmol of NaCl were mixed and dissolved in 45 mmol of OLAM under nitrogen atmosphere. The solution was heated at 553 K using a ramp of 15 K/min. Once the temperature reached 553 K, 15 mmol of OLAC were swiftly injected into the reaction flask. The reaction was held at 553 K for 1 h. After that time, the solution was naturally cooled down to room temperature. The product of the reaction was extracted by adding an excess of ethanol to the solution, followed by centrifugation at 4000 rpm for 10 min, after which the supernatant was discarded, and the precipitate was redissolved in n-hexane. This purification step was repeated three times. The rare earth oxide colloidal nanocrystals can be either stored in n-hexane or dried in an oven to form a solid product. The same methodology was applied also for the synthesis of 10 mol% Er^{3+} and 10 mol% Yb^{3+} doped Y_2O_3 nanocrystals by using 0.02 mmol $Er(Ac)_3{\cdot}H_2O$, 0.02 mmol $Yb(Ac)_3$ and 0.16 mmol of $Y(Ac)_3{\cdot}H_2O$. For the undoped Y_2O_3 nanocrystals, 0.2 mmol of $Y(Ac)_3{\cdot}H_2O$ were used, combined with NaCl. Following the same protocol, additional undoped Y_2O_3 nanocrystals were synthesized in the absence of NaCl structure-directing agent. The yields of the reactions are in the range from 85-95%.

2.3. Characterization

X-ray powder diffraction (XRPD) measurements were made using a Siemens D5000 diffractometer (Bragg-Brentano parafocusing geometry and vertical θ-θ goniometer) fitted with a curved graphite diffracted-beam monochromator, incident and diffracted-beam Soller slits, a 0.06° receiving slit and scintillation counter as a detector. The angular 2θ diffraction range was between 5 and 70°. The data were collected with an angular step of 0.05° at 3s per step and sample rotation. CuK_α radiation was obtained from a copper X-ray tube operated at 40 kV and 30 mA.

For the morphological characterization, transmission electron microscopy (TEM) images were acquired using a JEOL JEM-1011 electron microscope operating at an accelerating voltage of 100 kV or using a JEM-2100 high resolution transmission electron microscopy (HRTEM) operating at 300 kV. For the preparation of the grids, the nanocrystals were dispersed in n-hexane using ultrasounds and around 7 µL of the dispersion were deposited on the surface of a copper grid covered by a holey carbon film (HD200 Copper Formvar/carbon).

For the photoluminescence characterization of the nanodiscs, the emission spectra were recorded in a Yokogawa AQ6375 optical spectrum analyzer in the range from 450 nm to 750 nm, with a resolution of 2 nm and an integration time of 10 s. The nanodiscs were excited by a 980 nm emission fiber-coupled diode laser with different powers and the beam was focused on the sample using a 20x microscope objective (numerical aperture 0.4), bringing a spot size of approximately 10^{-6} m on the sample. The scattered excitation radiation was eliminated by using a 750 nm shortpass dichroic filter (Thorlabs). For the analysis of the temperature-photoluminescence dependence, the methodology was the same, except that the nanocrystals were located inside a heating stage (Linkam, THMS 600) equipped with a boron disk for improved temperature distribution.

III. Results and Discussion

3.1. Characterization of the nanodiscs

Er^{3+} and Yb^{3+} doped Y_2O_3 nanodiscs were synthesized *via* a digestive ripening-based process.[46] OLAC and OLAM were used as organic capping surfactants and NaCl as the structure-directing agent. The role of the injected OLAC is to remove the weakly bounded OLAM from the surface of the nanocrystals. OLAM was weakly bounded to the surface of nanoparticles, and OLAC exhibits a higher binding affinity,[47, 48] displacing OLAM from the surface and forming oleic acid coated nanoparticles. NaCl improves the crystallinity of the material, as it will be confirmed later with the XRD results.

Morphologically, the synthesized nanocrystals have the shape of nanodiscs self-assembled in fiber-like superstructures with lengths of micrometers (Fig. 1 (a) for undoped Y_2O_3). A possible explanation of this self-assembly arrangement relies of the combinatory effect of the van der Waals attractions and the steric repulsion of the oleate ligands capping the nanodiscs, as described elsewhere.[47, 49] Another possibility is that, as the nanodiscs were dispersed in an apolar solvent, the hydrophobic ligands tend to align the nanodiscs in these fiber-like structures on the TEM grids to minimize the boundary surface energy.[29] The nanodiscs have an average diameter of 22 ± 6 nm (Fig. 1 (b)), determined considering the width of the fiber-line structures in the TEM images. In addition, the inter-disc distance *i.e.* the distance between two individual nanodiscs (3.8 nm, Fig. 1 (c)), and the thickness of the discs (1 ± 0.2 nm, Fig. 1 (d)), could be determined through the HRTEM images. Fig. 1 (c), (d) also explain how the inter-disc distance and the thickness were determined.

When the dopants are introduced more independent discs are observed. Thus, in 4 mol% Er^{3+},4 mol% Yb^{3+} doped Y_2O_3 nanoparticles we can see a mixture of independent nanodiscs together with self-assembled nanodiscs in fiber-like structures (Fig. 1 (e)). The diameters of the nanodiscs are 28 ± 2 nm (Fig. 1 (f)). With the increase of the doping levels to 10 mol% Er^{3+} and 10 mol% Yb^{3+}, even more independent nanodiscs could be observed (Fig. 1 (g)). In addition, also the diameter of the nanodiscs increased up to 30 ± 2 nm (Fig. 1 (h)). Thus, with the introduction of the dopants, the diameters of the nanocrystals increased, and they seem to have more problems to arrange themselves into fiber-like structures. A reason for that might be that the dopants disturb the lattice arrangement of host.[50] Thus, it seems that the introduction of dopants also affects to the arrangement of the nanodiscs into fiber-like structures.

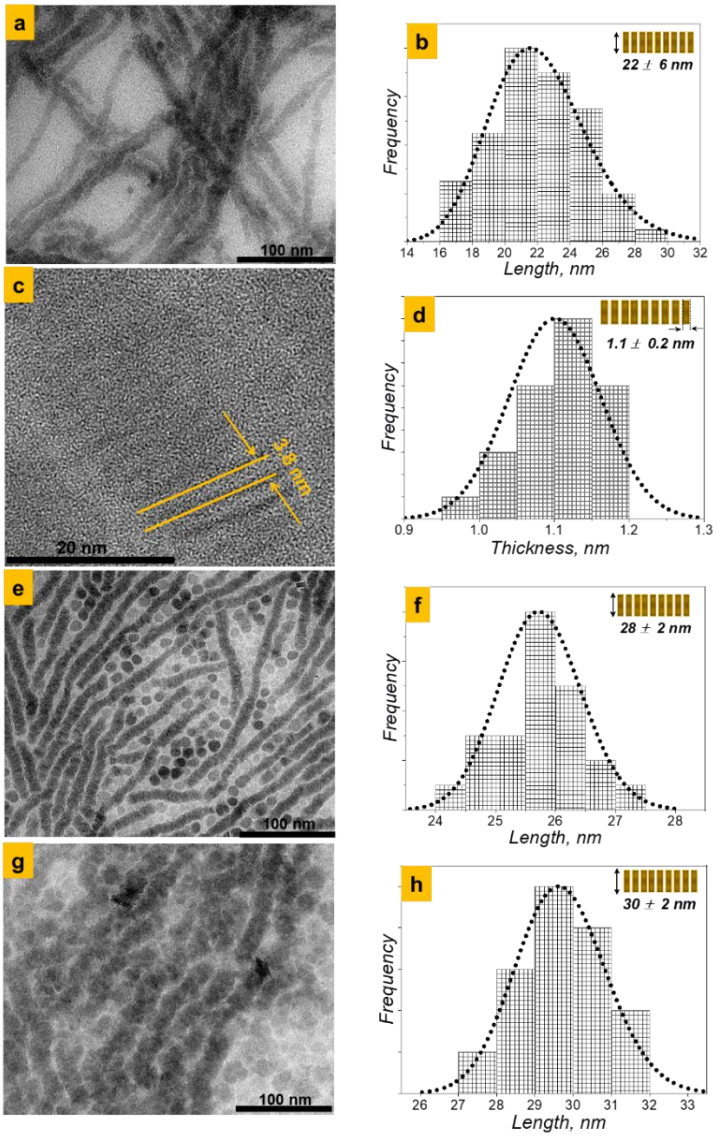

Fig. 1. TEM/HRTEM images and the lognormal diameter length distribution of: (a) and (b) undoped Y_2O_3; (c) and (d) HRTEM image of undoped Y_2O_3 nanodics for determination of the inter-disc distance and the disc thickness; (e) and (f) 4

mol% Er^{3+},4 mol% Yb^{3+}; and (g) and (h) 10 mol% Er^{3+},10 mol% Yb^{3+} doped Y_2O_3 nanodiscs synthesized *via* a digestive ripening-based synthesis directed by NaCl.

The structure of all the colloidal nanodiscs was identified to belong to the cubic phase of yttrium oxide with space group *Ia* $\bar{3}$ (Fig. 2 (a)). However, the introduction of dopants affected their crystallinity, as the intensity of the diffraction peaks decreased (Fig. 2 (a)). This effect was accentuated as the concentration of dopants increased. A general trend observed in the XRPD patterns of the ultrathin rare earth oxide nanocrystals is the significant broadening of the peaks, as reported previously.[36, 47, 51] Moreover, these broad peaks are shifted towards lower angle values if compared with the bulk reference pattern, as previously stated.[36, 47, 51] A possible reason for this behavior could be related to an expansion of the crystallographic net due to the strong one dimensional (1D) confinement in the crystallographic planes.[36, 47, 51]

The absence of some of the reflections is expected in thin disc morphologies, since their anisotropic shape makes that a limited number of planes become available to diffract, which resulted in a reduced number of diffraction peaks in the XRPD patters recorded.[29] Also, the rather low synthesis temperature (553 K) results in a poor crystallinity of the product obtained, and probably also, in a distorted unit cell of the cubic yttrium oxide structure, although this last point was not verified in the present structures. Taking into account previous results,[36, 47, 51] the presence or the absence of the (400) peak, can be an indication of the crystallographic orientation of the morphologies observed. When the obtained morphology are the self-assembled nanodiscs, the (400) peak is clearly absent (Fig. 2 (a)). This would indicate that the main plane of the nanodiscs corresponds to the (100) plane, and the radial growth direction corresponds to the [110] one. As can be seen, by comparing the XRPD patterns in Fig. 2 (a) and that of the same product synthesized without NaCl (Fig. S1 in the Supporting Information), the use of NaCl during the synthesis process improves substantially the crystallinity of the products obtained.

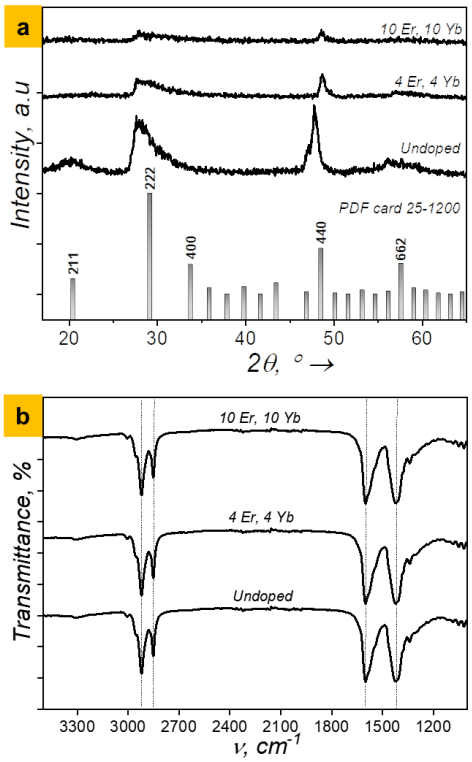

Fig. 2. (a) XRPD patterns and (b) FT-IR spectra of the undoped, 4 mol% Er^{3+}, 4 mol% Yb^{3+}, and 10 mol% Er^{3+},10 mol% Yb^{3+} doped Y_2O_3 nanodiscs synthesized *via* digestive ripening-based synthesis directed by NaCl. Within (a), the reference pattern of the cubic yttrium oxide (PDF card 25-1200) is included for comparison.

The dried nanodiscs were also characterized using Fourier Transform Infrared (FT-IR) (Fig. 2 (b)). The spectra reveal that in all cases, the final purified nanodiscs contain moieties of oleic acid. No traces of the -NH_2 stretching band of OLAM or the -C=O characteristic stretching band of OLAC are detected. Additionally, two characteristic bands at 1605 cm^{-1} and 1420 cm^{-1}, ascribed to the antisymmetric and symmetric stretching vibrations of the deprotonated carboxylic group (COO^-), indicate that OLAC molecules were deprotonated, chemisorbed and transformed into carboxylates anions due to the promotion from OLAM.[52] The difference

between these two bands (185 cm^{-1}) reveals that the coordination of the carboxylate ions to the yttrium oxide structure is of bridging or ionic type, as previously reported.[53] It is assumed that these oleic acid moieties are coating the surfaces of the nanodiscs. Besides, there is no great influence of the doping in the final surface of the nanodiscs.

3.2. Upconversion luminescence of the nanodiscs

The photoluminescence generated by these Er^{3+},Yb^{3+} doped Y_2O_3 nanodiscs, was recorded within the wavelength range from 450 nm to 750 nm, after exciting the nanoparticles with NIR 980 nm wavelength. The UC emissions consisted of two bands generated by Er^{3+}: the green band composed by the emissions arising from the $^2H_{11/2} \rightarrow {}^4I_{15/2}$ and $^4S_{3/2} \rightarrow {}^4I_{15/2}$ transitions, centered at 525 nm (labelled as *H*) and 550 nm (labelled as *S*), respectively; and the red band centered at 660 nm, attributed to the $^4F_{9/2} \rightarrow {}^4I_{15/2}$ transition (Fig. 3 (a)).

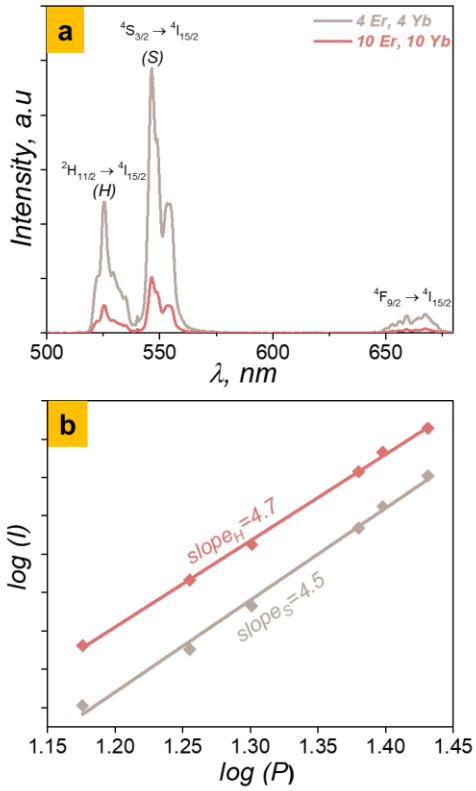

Fig. 3. (a) UC emission bands of Er^{3+}, Yb^{3+} doped Y_2O_3 nanodiscs, and (b) Variation of the intensity of the green emissions with the power of the 980 nm laser.

Comparing the intensity of the luminescence achieved from the different doping levels of Er^{3+} and Yb^{3+} investigated, 4 mol% Er^{3+} and 4 mol% Yb^{3+} doped nanoparticles exhibit the highest intensity (Fig. 3 (a)). On the other hand, for the sample doped with 10 mol% Er^{3+} and 10 mol% Yb^{3+}, a drastic reduction of the intensity of all the emissions is detected (Fig. 3 (a)) due to concentration quenching.[49, 54] On the contrary of the results presented by Degelsen *et al.*[49] in which they observed a reduced concentration quenching in the Eu^{3+}:Y_2O_3 nanoparticles, for Er^{3+},Yb^{3+}:Y_2O_3 nanodiscs, quenching by concentration is present. This fact might be due to the partial loss of the self- assembling character in the 10 mol%, Er^{3+}, 10 mol% Yb^{3+} particles (Fig. 1 (g)), therefore the Er-Er average distance is not affected by the order of the self-assembly. Then, the behaviour that should be expected is the usual one considering only the Er-Er intradisc distance. In the case of Degelsen *et al.* the reduced concentration quenching was attributed to the fact that the significant Eu-Eu distance for the energy transfer among the ions, was affected by the presence of ligands on the surfaces of the nanocrystals, then, giving a distance around 3.8 nm, which is larger than the critical distance for energy transfer among active ions.[49]

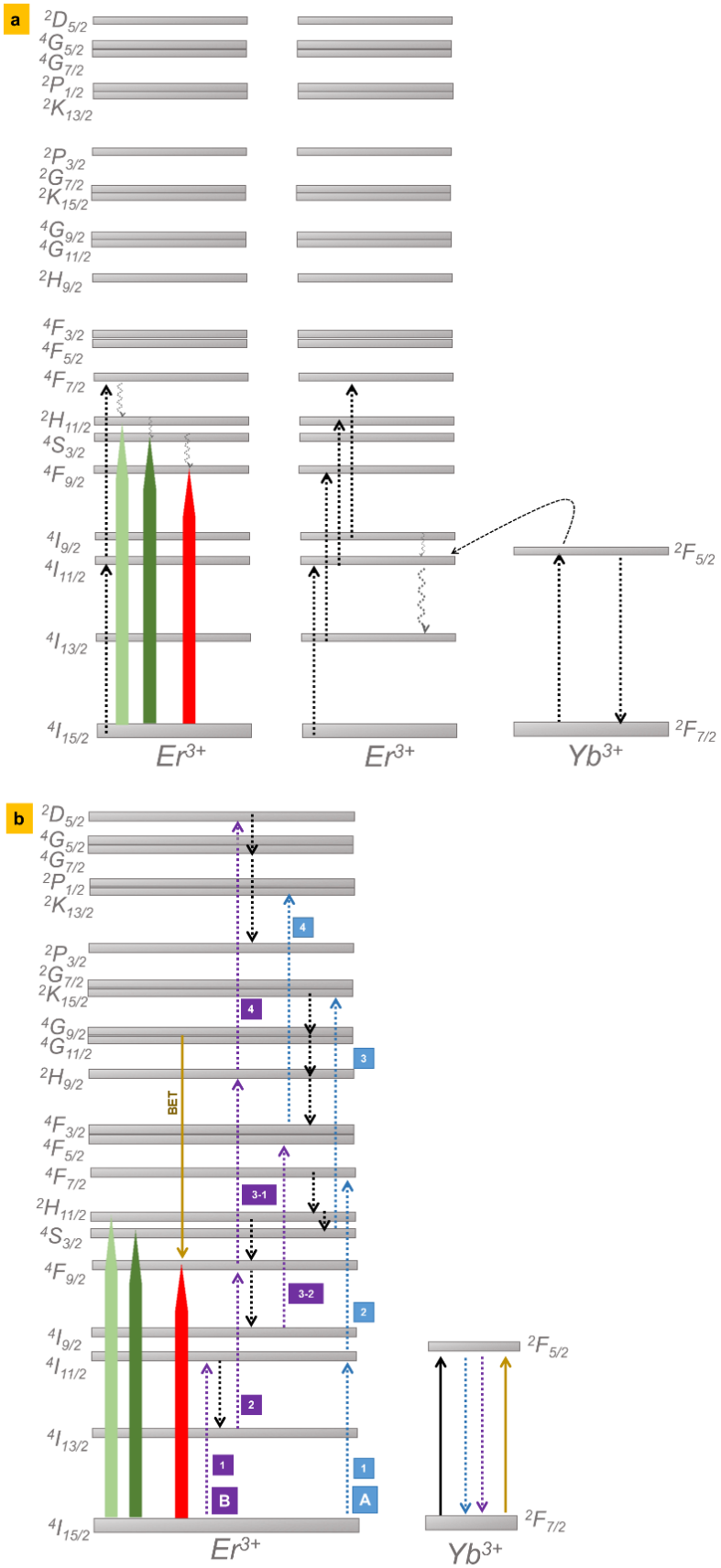

Fig. 4. Four photon absorption process for the generation of the upconversion emission bands of Er^{3+}, Yb^{3+} doped Y_2O_3 nanodiscs: (a) classic mechanism, and (b) new mechanism under high power densities following two pathways (A in blue, and B in magenta).

The mechanism to explain the generation of these UC emission lines, can be deduced by determining the number of pumping photons involved in the UC process. In order to determine this number, the slope of a linear fit obtained from the relationship between the intensity of the emissions versus the pumping power in a log-log plot, should be calculated. This relationship is expressed as:[55]

$$I_{UC} \propto P^n \qquad (1)$$

where I_{UC}, P and n stand for the intensity of the UC emissions, the power of the pumping laser, and the number of photons involved in the UC mechanism. This slope, while exciting the nanocrystals with a 980 nm laser diode, is around four (Fig. 3 (b)) for both *H* and *S* emission bands. This is surprising, since normally a slope around 2 is reported mainly in Er^{3+} doped systems for these emissions.[16] This characterization was repeated several times to confirm this result, and in all cases, always a slope around 4 was obtained.

Thus, apparently, these nanodiscs need to absorb 4 photons at 980 nm to generate the green luminescence. This four-photon assisted process occurs *via* the energy transfer (ET) from Yb^{3+} (the sensitizer) ions to the fluorescent Er^{3+} (the activator) ions. Yb^{3+} ion is an efficient sensitizer since it exhibits a strong absorption band at around 980 nm, assigned to the $^2F_{7/2} \rightarrow {}^2F_{5/2}$ transition. This excited state is resonant in energy with the $^4I_{11/2}$ state of Er^{3+}, allowing in this way a successful ET between these ions (Fig. 4 (a)).[56] Normally, in a two photon absorption process, Er^{3+} would be excited to its $^4F_{7/2}$ state *via* two successive ET processes from Yb^{3+} ions in close proximity, promoting it from its ground state ($^4I_{15/2}$) to the intermediate state ($^4I_{11/2}$) and subsequently to the excited state ($^4F_{7/2}$). From this excited state, the ions can decay non-radiatively to the $^2H_{11/2}$ and $^4S_{3/2}$ lower-lying levels, from which by relaxing back to the ground state, leads to the generation of the green emissions centered at 525 nm and 550 nm, respectively (Fig. 4 (a)). Alternatively, the $^4F_{9/2}$ state of Er^{3+} can be populated *via* a non-radiative decay from the $^4F_{7/2}$ excited level or from a cross relaxation process between Er^{3+} and Yb^{3+} like $^4F_{7/2}$,$^4I_{11/2} \rightarrow {}^4F_{9/2}$,$^4F_{9/2}$. From the $^4F_{9/2}$ state, a radiative relaxation process back to the $^4I_{15/2}$ ground state, generates the red emission of this ion centered at 660 nm (Fig. 4 (a)).[54, 57]

Nevertheless, in the four photons absorption process depicted in Fig. 4 (b), two differrent pathways might occur, either populating the $^2K_{13/2}$ level of Er^{3+}, as depicted in pathway A (blue color in Fig. 4 (b)) or populating the $^2D_{5/2}$ level of Er^{3+}, as depicted in pathway B (magenta color in Fig. 4 (b)). Probably, from these levels, violet and blue emissions might be generated, as reported previously in Er^{3+}, Yb^{3+}:Y_2O_3 nanocrystals [57], however, due to the range of detection of the photodetector used to record the spectra, these emissions could not be seen in our case. These mechanisms should be verified in the future by extending the detection range of the detector. Even if these emissions are generated, several non-radiative processes should occur to populate the $^2H_{11/2}$, $^4S_{3/2}$ and $^4F_{9/2}$ lower-lying levels, from which by relaxing back to the ground state, leads to the generation of the green emissions centered at 525 nm and 550 nm, and the red emission centered at 660 nm respectively (Fig. 3 (c)).

Four-photon UC emission of Er^{3+} has been reported previously for Er^{3+},Yb^{3+}:Y_2O_3 nanocrystals at high Yb^{3+} concentrations (10 mol% Yb^{3+} *vs* 1 mol% Er^{3+}), generating blue (409 nm) and violet (390 nm) emissions, assigned to the $^2H_{9/2} \rightarrow {}^4I_{15/2}$ and $^4G_{11/2} \rightarrow {}^4I_{15/2}$ transitions.[58] This effect was attributed to an enhancement of the UC rate caused by the average reduction of the distance between the Yb^{3+} and the Er^{3+} ions when the Yb^{3+} concentration increased. In fact, in our case, the high ratio of Yb^{3+} per Er^{3+} that can be encountered in the structure of the nanosdiscs with the doping concentrations used, would explain this four-photon UC emission mechanism. Furthermore, this would also explain the severe luminescence quenching observed for the nanodiscs doped with 10 mol% Er^{3+} and 10 mol% Yb^{3+}.

More recently, multiband UC luminescence has been reported for Er^{3+} doped microcrystals exited at high powers with material alteration.[59] Through a complex setup build to trap single microcrystals in solution, and record time-resolved luminescence at the nanosecond scale in Er^{3+},Yb^{3+}:$NaYF_4$ microcrystals, the authors were able to demonstrate two different pathways for the four-photon UC emission process that allows populating the high energy $^2D_{5/2}$ and $^2K_{13/2}$ levels of Er^{3+} (Fig. 4 (b)). They were able to demonstrate that although one of the pathways (that allowing to populate the $^2K_{13/2}$ level: pathway A in Fig. 4 (b)) is more efficient than the other, one can promote the other by non-radiative relaxation and back energy transfer (BET) processes. In that case, despite the concentration of Er^{3+} and Yb^{3+} ions are the traditional one optimized to maximize the emission intensity in these crystals (1 and 20 mol%, respectively), the authors needed to use a high excitation power density of 2.3 MW cm^{-2}. In our case, these results would imply that a new mechanism of population of the $^2H_{11/2}$ and $^4S_{3/2}$ levels can occur, through the population of the high energy $^2D_{5/2}$ and $^2K_{13/2}$ levels, followed by a non-radiative relaxation towards the $^2H_{11/2}$ and $^4S_{3/2}$ levels, as proposed in Fig. 4 (b).

However, in our case, no such high excitation power densities had to be used (~800 W cm^{-2}), probably due to the similar concentration of Er^{3+} and Yb^{3+} ions applied. However, this would imply also the generation of a high amount of heat in our nanodiscs, making them very inefficient from the point of view of light generation (although would have other interesting applications as photothermal conversion agents in applications in which an efficient conversion from light to heat is required, not investigated here for being out of the scope of the present paper). This large generation of heat, would also allow us to explain the difficulties we encountered to use these nanodiscs as primary luminescent thermometers, as will be explained later in Section 3.4. The results obtained in the characterization of 4 mol% Er^{3+} and 4 mol% Yb^{3+} doped Y_2O_3 nanodiscs as primary luminescent would indicate that the most plausible mechanism for the excitation of Er^{3+} to generate green light is that one proposed in Fig. 4 (b), induced in that case by the concentrations of Er^{3+} and Yb^{3+} ions used.

3.3. Luminescence nanothermometry of Er^{3+}, Yb^{3+}:Y_2O_3 nanodiscs

Er^{3+}, Yb^{3+}:Y_2O_3 nanodiscs could be applied as luminescence nanothermometers based on two green emissions of Er^{3+} ions from the 4 mol% Er^{3+} and 4 mol% Yb^{3+} doped particles. Using the ratio among the intensities of the two emission bands in the green, the thermometric parameter (Δ) or fluorescence intensity ratio (FIR), can be described as:[60]

$$\Delta = FIR = \frac{I_H}{I_S} = B \exp\left(-\frac{\Delta E}{k_B T}\right) \qquad (2)$$

where I_H and I_S stand for the integrated intensity of the two green emissions arising from the $^2H_{11/2}$ and $^4S_{3/2}$ emitting levels, respectively; B is the pre-exponential constant; ΔE is the energy gap between the $^2H_{11/2}$ and $^4S_{3/2}$ levels in the particular host; k_B is the Boltzmann's constant; and T is the absolute temperature.

The performance of the 4 mol% Er^{3+} and 4 mol% Yb^{3+}:Y_2O_3 upconverting nanodiscs as luminescent nanothermometers, was investigated by analyzing the effect of the increase of temperature in the range from 298 to 338 K on the intensity ratio of the emissions arising from these two thermally coupled electronic levels of Er^{3+} after exciting the nanodiscs with a 980 nm laser operating with a power density of approximately 800 W cm^{-2}. Fig. 5 (a) shows the temperature dependence of the intensity of the green emissions of these Er^{3+}, Yb^{3+}:Y_2O_3 nanodiscs in this range of temperatures. By increasing the temperature, the intensity of the 550 nm emission decreases, while the intensity of the 525 nm emission is slightly increasing ~~nearly constant~~ (Fig. 5 (b)).

The FIR is proportional to the change of temperature (Fig. S2 at Supporting Information). Eq. 2 can be rewritten in the logarithmic form as:[60]

$$\ln(\Delta) = \ln(FIR) = \ln(B) + \left(\frac{\Delta E}{k_B T}\right) = \ln(B) + \left(-\frac{C}{T}\right) \qquad (3)$$

where B and C stands for constants to be determined from the linear fitting expressed in Eq. 3 (Fig. 5 (c)). From this fitting, the values of the slope (990.59 ± 24.14) and the intercept (2.51 ± 0.076) are deduced. Knowing these values, it was possible to extract the value of the pre-exponential term B and the energy gap ΔE between the Er^{3+} $^2H_{11/2}$ and $^4S_{3/2}$ thermally coupled levels, and furthermore, determine the thermometric performance of the self-assembled nanodiscs. The corresponding value of B and ΔE are 12.30 and 688 cm^{-1}, respectively.

The thermometric performance of these nanodiscs can be evaluated by using the absolute thermal sensitivity (S_{abs}), the relative thermal sensitivity (S_{rel}), and the temperature resolution (δT).[1, 60] S_{abs} is dependent on the acquisition setup, and it is defined as:

$$S_{abs} = \left|\frac{\partial \Delta}{\partial T}\right| = B * \frac{\Delta E}{k_B T^2} \exp\left(-\frac{\Delta E}{k_B T}\right) = \frac{\Delta * slope}{T^2} \qquad (4)$$

Knowing the value of the slope from Eq. 3, the maximum value of S_{abs} is around 0.0057 K^{-1} at 338 K (Fig. 5 (d)). S_{abs} is continuously increasing with the increase of temperature (Fig. 5 (d)). However, the figures of merit normally used to compare the performance of nanothermometers, independently of their nature, are the relative thermal sensitivity (S_{rel}) and the temperature resolution (δT).[1, 60] The relative thermal sensitivity of the Er^{3+}, Yb^{3+}:Y_2O_3 upconverting nanodiscs is expressed as:[60]

$$S_{rel} = \frac{1}{\Delta}\left|\frac{\partial \Delta}{\partial T}\right| * 100\% = \frac{\Delta E}{k_B T^2} * 100\% \qquad (5)$$

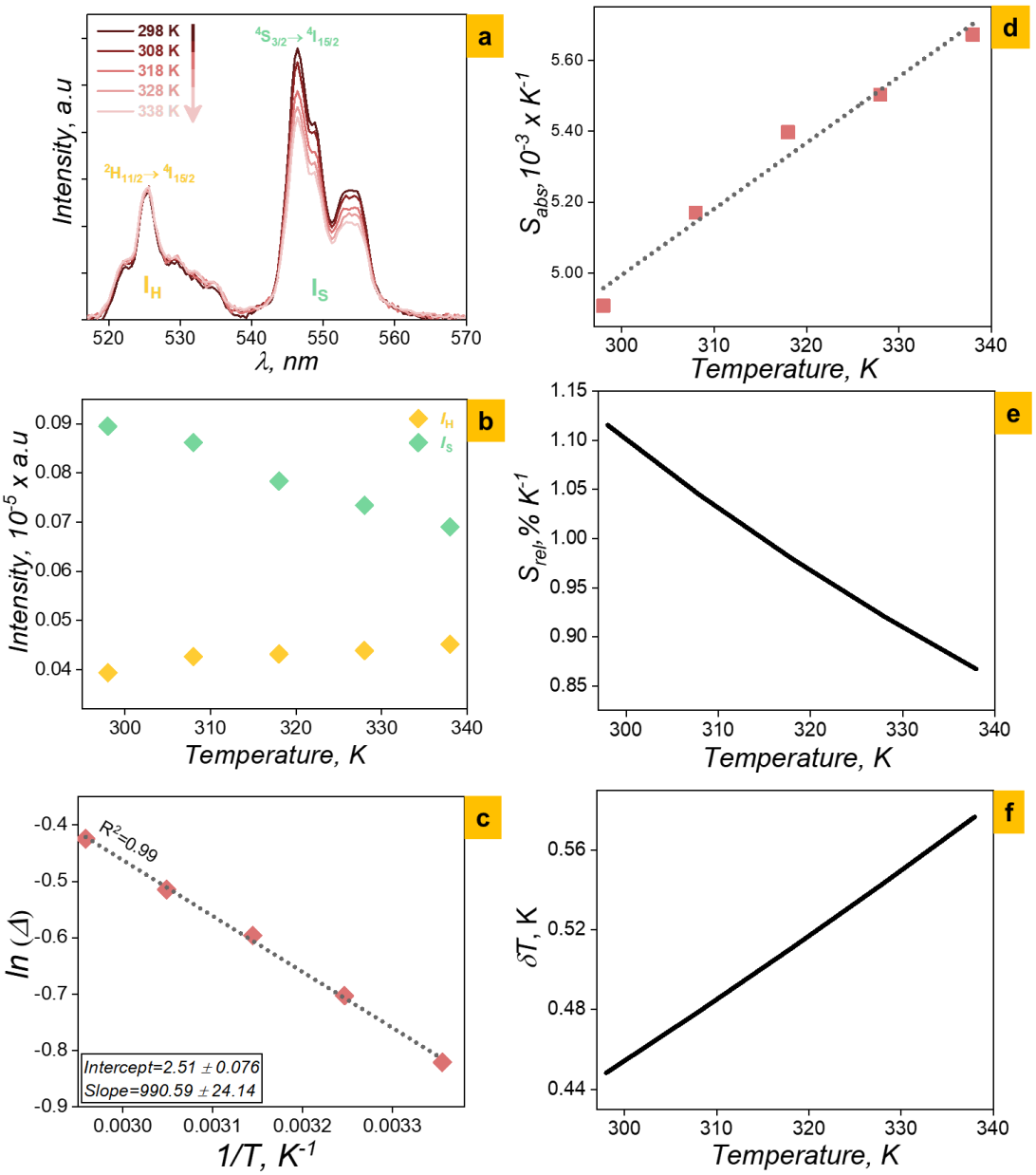

Fig. 5. (a) Temperature dependence of the intensity of the green emissions bands of the Er^{3+}, Yb^{3+}:Y_2O_3 upconverting nanodiscs. (b) Variation of the integrated emission intensities with temperature. (c) Plot of the natural logarithmic of Δ as a function of the inverse of temperature. (d), (e), and (f) absolute thermal sensitivity, relative thermal sensitivity and temperature uncertainty of the nanodiscs as a function of the temperature, respectively.

This relative thermal sensitivity is 1.11% K^{-1} at room temperature for our nanodiscs. The evolution of S_{rel} as a function of temperature is depicted in Fig. 5 (e). S_{rel} displays an inverse relationship with the temperature: as the temperature increases, the values of S_{rel} decrease gradually.

The temperature resolution of the nanothermometers is expressed as:[60]

$$\delta T = \frac{1}{S_{rel}} \frac{\delta \Delta}{\Delta} \qquad (6)$$

where $\frac{\delta \Delta}{\Delta}$=0.5% is an example of the relative error of the optical setup in the determination of the thermometric parameter.[1] The calculated temperature resolution of the Er^{3+}, Yb^{3+}:Y_2O_3 upconverting nanodiscs is 0.44 K at 298 K, that increases up to 0.57 K at 338 K (Fig. 5 (f)).

Table 1. Thermometric performance of Er^{3+}, Yb^{3+} doped nanothermometers based on the intensity ratio between the green emissions of Er^{3+} ions assigned to the $^2H_{11/2}\rightarrow{}^4I_{15/2}$ and $^4S_{3/2}\rightarrow{}^4I_{15/2}$ transitions. λ_{exc} and λ_{em} stand for the excitation and the emission wavelengths. ΔT is the temperature interval where the performance of these nanothermometers was analyzed. The highest values of the relative thermal sensitivity S_{rel} and temperature uncertainty δT are reported, together with temperature where these values were obtained. In asterisk (*), values calculated from us, using the data provided at the corresponding articles under "Reference" column.

Host	λ_{exc} (nm)	λ_{em} (nm)	ΔT (K)	S_{abs}/T (K^{-1}/K)	S_{rel}/T (%K^{-1}/K)	δT (K)	Reference
Y_2O_3 microtubes	980	525, 550	280-700	0.0078/625	1.57*/280	0.32*	[61]
$LiNbO_3$	980	530, 550	285-453	0.0075/310	1.53*/285	0.33*	[62]
$YMoO_4$@SiO_2	980	531, 552	300-368	0.0235/368	1.41*/300	0.35*	[63]
$Gd_2(MoO_4)_3$	980	525, 545	295-660	Not reported	1.34/295	0.37*	[64]
Y_2O_3 flakes	980	522, 563	298-573	0.0050/563	1.28*/298	0.39*	[25]
$LaGdO_3$	980	530, 550	283-393	0.0034/393	1.27/283	0.43	[65]
$Gd_6O_5F_9$	980	527, 547	300-523	0.0057/498	1.23/300	0.40*	[66]
$GdVO_4$	980	525, 553	303-453	0.0125/453	1.20/303	0.41	[16]
$LuVO_4$@SiO_2	915	524, 553	303-353	0.0057/353	1.17/303	0.43*	[67]
Y_2O_3 nanodiscs	**980**	**525, 550**	**298-338**	0.0057/338	**1.11/298**	**0.44**	**This work**
Al_2O_3	978	523, 545	295-973	0.0051/495	1.10*/295	0.45*	[68]
$BaWO_4$/g-C_3N_4	980	524, 551	293-393	0.0107/293	1.06/393	0.47*	[69]
Y_2O_3 nanoparticles	980	523, 553	323-573	0.0194/543	1.04/323	0.48*	[70]
$BaMoO_4$	980	531, 552	303-523	0.0227/463	1.03*/303	0.48*	[71]
β-$NaYF_4$@SiO_2	980	520, 550	300-900	Not reported	1.02/300	0.49*	[72]
ZnO-$CaTiO_3$	980	524, 545	311-700	0.0086/311	1.01/311	0.50*	[73]
$SrWO_4$	980	525, 547	300-518	0.0149/403	0.96*/300	0.52*	[74]
$GdVO_4$@SiO_2	980	520, 550	297-343	0.0101/343	0.94/343	0.40	[75]
La_2O_3	980	523, 548	303-600	Not reported	0.91/303	0.55*	[76]
YAG	980	522, 563	298-573	0.0017/404	0.90*/298	0.55*	[25]
YVO_4	980	524, 554	300-485	0.0116/380	0.86*/300	0.58*	[77]
Gd_2O_3	980	523, 548	300-900	0.0039/300	0.83*/300	0.60*	[78]
$NaY(WO_4)_2$	980	530, 552	293-503	0.0060/293	0.77*/293	0.65*	[79]
$LaAlO_3$	980	522, 563	298-573	0.0032/404	0.65*/298	0.77*	[25]
$La_2Ti_2O_7$	980	529, 553	333-553	0.0057/550	0.63/333	0.44	[80]
Y_2O_3/α-Al_2O_3 spheres	980	520, 564	273-773	Not reported	0.60/273	0.60	[81]
Y_2SiO_5	975	530, 550	300-600	0.0070/650	0.14*/300	3.57*	[82]

Table 1 compares the relative sensitivity and the temperature resolution of different luminescent nanothermometers based also on the green emissions of Er^{3+}, together with information such as type of host, excitation wavelength, precise location of the green emissions, the temperature range from which their performance was evaluated.[25, 69, 71, 73-75, 77, 79-82] Table 1 also includes S_{abs} for all the hosts compared. Ciric *et al.*[83] developed a method to calculate theoretically the figures of merit of luminescent thermometers operating under the FIR scheme, considering the Judd-Ofelt parameters, refractive index, Slater integrals, spin-orbit parameters, reduced matrix elements, and energy differences between emitting levels used for FIR. The tendency they predicted for the values of S_{abs} as a function of the host used for Er^{3+} ions, matches the tendencies we observe for the "experimental" values determined using Eq. 4 reported in the literature for these hosts. So that, molybdates, tungstates, vanadates and simple oxides show the highest values of S_{abs}. For the case of the Y_2O_3 nanodiscs presented in this paper, the value we report of S_{abs} is far below the maximum possible value predicted by Ciric *et al.* 0.0181 K^{-1}.[83] However, the range of temperatures analyzed in this paper (up to 338 K) is substantially lower than that for which, theoretically, the maximum S_{abs} should be achieved (619 K).

The performance of the Y_2O_3 nanodiscs, in terms of S_{rel} and δT is similar to that obtained with particles of Y_2O_3 with other shapes, with the exception of the combination of Y_2O_3 with α-Al_2O_3 in the form of spheres, in which probably a different host should be considered. In terms of S_{abs}, that also marks how intense are the emissions arising from the $^2H_{11/2}$ level (the greatest the S_{abs} value, the higher the intensity of the emission arising from this level),[83] their performance is similar to that of Y_2O_3 flakes, although in this case, S_{abs} is achieved at much higher temperatures. The same happens with Y_2O_3 microtubes, that despite showing a slightly higher S_{abs}, it is also achieved at substantially higher temperatures than those investigated in this paper. When compared with Y_2O_3 nanoparticles, the S_{abs} achieved by our nanodiscs is almost one quarter of that reported for Y_2O_3 nanoparticles, however, the temperature at which this value was reported is more than 200 K higher. According to that, our nanodiscs seem to perform relatively well when compared with Y_2O_3 particles with other shapes.

Fig. S3 in the Supporting Information shows the relative thermal sensitivity of all these Er^{3+} based luminescent thermometers, clearly indicating the position of our 4 mol% Er^{3+} and 4 mol% Yb^{3+} doped Y_2O_3 nanodiscs. Compared to the rest of the luminescent thermometers reported here,[16, 25, 62-68, 76, 78, 81] our nanodiscs have a small size, which is a prerequisite for the selection of nanothermometers for biomedical applications, as this characteristic guarantees an effective excretion of the nanoparticles after their implementation in biological mediums, avoiding in this way possible toxicity.[1]

3.4. Testing Er^{3+}, Yb^{3+}:Y_2O_3 nanodiscs as primary luminescent thermometers

The thermally coupled nature of the erbium electronic levels allows to explore the possibility of using these nanocrystals as potential primary luminescent thermometers, where the absolute temperature calibration is predicted independently of the medium, and the thermometric parameter is based on a known equation of state (the Boltzmann equation in this case).[45] Thus, a primary thermometers would avoid the time consuming tasks of multiple re-calibration in different media.[45]

From Eq. 2, the absolute temperature can be determined as:[60]

$$T_{abs} = \frac{\Delta E_0}{k_B} \frac{1}{ln\left(\frac{B_0}{\Delta_0}\right)} \qquad (7)$$

In order to have the equation of state for the primary luminescent thermometer, the value of the energy gap ΔE_0 between the energy levels from which the green emissions arise, and the value of the thermometric parameter at no-laser power (Δ_0), should be calculated for the nanodiscs by independent measurements and not as fitted parameters of Eq. 2, as pointed out elsewhere.[45]

The energy gap ΔE_0 between the $^2H_{11/2}$ and $^4S_{3/2}$ levels in yttrium oxide colloidal nanodiscs is derived by deconvolution of the emission spectra at room temperature (298 K) by a set of Lorentz peaks and evaluating the position of the barycenter's of the $^2H_{11/2} \rightarrow {}^4I_{15/2}$ and $^4S_{3/2} \rightarrow {}^4I_{15/2}$ transitions (Fig. 6 (a)). By following this methodology, the value of ΔE_0 between these two levels was calculated to be 776 ± 3 cm^{-1}. the value of ΔE_0 remains almost constant upon increasing the excitation power (Fig. S4 in the Supporting Information), whereas the intensity of the two green emission lines is proportional to the change of the excitation power (Fig. 6 (b)).

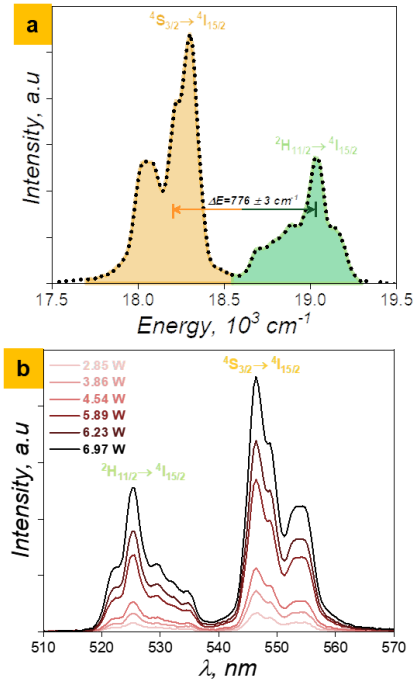

Fig. 6. (a) Determination of the energy gap ΔE_0 between the emissions arising from the Er^{3+} $^2H_{11/2}$ and $^4S_{3/2}$ levels in 4 mol% Er^{3+} and 4 mol% Yb^{3+} doped Y_2O_3 nanodiscs. (b) Variation of the intensity of the green emission bands with the power of the 980 nm laser.

The value of the thermometric parameter Δ_0 at no-laser excitation (no laser-heating) and the corresponding B_0 pre-exponential factor can be determined from the plot of Δ *versus* the excitation laser power by extrapolating the linear fit to the limit of zero excitation laser power.[45] In general, the variation of the thermometric parameter with the increase of the excitation power, obeys to a linear relationship (Fig. 7 (a)). The intercept, *i.e.* the thermometric parameter Δ_0 at no-laser excitation, is 0.30055 ± 0.02. By applying Eq. 7 with T=298 K, the value of the pre-exponential parameter B_0 is calculated as 12.74. This value is close to the value that can be calculated from the Judd-Ofelt parameters using the expression:[84]

$$B_0 = \frac{0.7158\,\Omega_2 + 0.4138\,\Omega_4}{0.2225\,\Omega_6} + \frac{0.0927}{0.2225} \qquad (8)$$

where Ω_2, Ω_4 and Ω_6 are the Jud-Ofelt parameters.

Using Ω_2=5.34 ·10^{-20} cm^2, Ω_4=1.63 ·10^{-20} cm^2 and Ω_6=0.59 ·10^{-20} cm^2, coefficient determined for the emitting ion within yttrium oxide host,[85] a value of B_0 of 12.34 is calculated.

In addition, in the limit of the zero-excitation laser power, the temperature of the material, T_0, corresponding to no laser-heating effect, can be calculated from Eq. 7 as:[45]

$$T_0 = \frac{\Delta E_0}{k_B} \frac{1}{\ln\left(\frac{B_0}{\Delta_0}\right)} \qquad (9)$$

This temperature is calculated as 298.99 K.

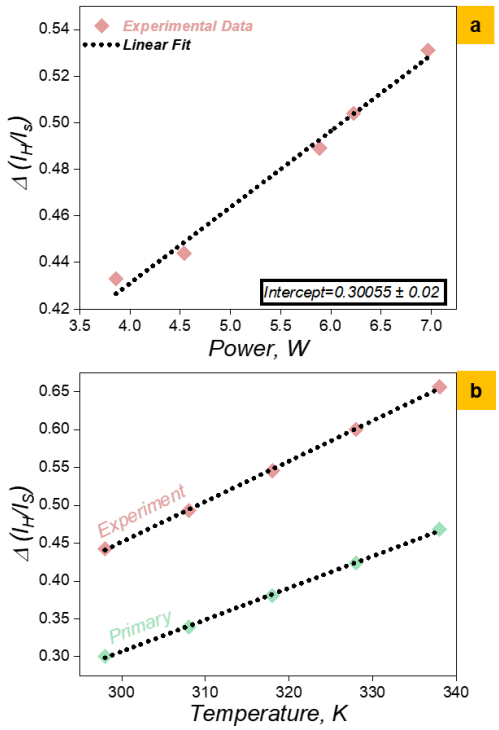

Fig. 7. (a) Room temperature variation of the thermometric parameter with the excitation power. (b) Calculated absolute temperature using Eq. 7 *versus* the experimental temperature determined from the emission spectra generated by the 4 mol% $Er^{3+}$and 4 mol% Yb^{3+} doped Y_2O_3 nanodiscs using laser power density of 800 W cm^{-2}.

The absolute temperature T_{abs} can be determined by the ratio Δ/Δ_0 using Eq. 2 and Eq. 7:

$$\frac{1}{T_{abs}} = \frac{1}{T_0} - \frac{k_B}{\Delta E_0} ln\left(\frac{\Delta}{\Delta_0}\right) \qquad (10)$$

Thus, the expressions for the thermometric parameter for the primary luminescent thermometer and the secondary one derived from the experimental determination of the temperature from the spectra of Er^{3+} in 4 mol% Er^{3+} and 4 mol% Yb^{3+} doped Y_2O_3 nanodiscs are:

$$\Delta = 12.74 \exp\left(-\frac{776}{k_B T}\right) \quad (11)$$

$$\Delta = 12.30 \exp\left(-\frac{688}{k_B T}\right) \quad (12)$$

Their variation with the temperature in the ranges from 298-338 K are plotted in Fig. 7 (b). Significant differences are observed between the absolute and the experimental temperature. The fact that the experimental Δ line is above the Δ_0 line, indicated that there is a systematic heating of the nanodiscs, as we demonstrated previous for the heating effect generated by the different excitation powers in Er^{3+}, Yb^{3+}:$GdVO_4$ samples.[16] The origin of this heat might be the four-photon upconversion mechanism observed for these 4 mol% Er^{3+} and 4 mol% Yb^{3+} doped Y_2O_3 nanodiscs (Section 3.2), and the important amount of energy released in the form of heat from the non-radiative associated processes to populate the $^2H_{11/2}$ and $^4S_{3/2}$ electronic levels of Er^{3+} from higher energy levels, despite blue or violet emissions could not be observed because of the spectral range measured in this case.

This drawback might be overcome by reducing the excitation power used, but this action restricts the intensity of the emission lines used for luminescent nanothermometry, since the signal to noise ratio would decrease substantially. Thus, this would be evidence that not all UC materials can be used as primary luminescent thermometer, as suggested previously.[45] The intrinsic nature of the material, in some cases, as it happens here for the concentrations of doping ions used and size of the nanocrystals, prevent their use for this purpose by the UC light generation mechanism involved, that imply the release of an important quantity of heat.

IV. Conclusions

Ultrathin self-assembled Er^{3+}, Yb^{3+} doped Y_2O_3 nanodiscs were synthesized *via* a digestive ripening reaction in the presence of organic surfactants (oleic acid and oleylamine) and the structure-directing agent NaCl. 4 mol% Er^{3+}, 4 mol% Yb^{3+} and 10 mol% Er^{3+}, 10 mol% Yb^{3+} doped Y_2O_3 exhibit emissions upon 980 nm excitation in the green and the red. A severe concentration quenching effect was observed for the 10 mol% Er^{3+}, 10 mol% Yb^{3+} doped Y_2O_3. A four-photon UC mechanism was determined for the 4 mol% Er^{3+}, 4 mol% Yb^{3+} doped Y_2O_3 nanodiscs, which would imply that the $^2H_{11/2}$ and the $^4S_{3/2}$ energy levels of Er^{3+} are populated from non-radiative relaxation processes from higher energy levels. These nanodiscs were tested as potential luminescent nanothermometers based on the intensity ratio of the green emissions, exhibiting a maximum relative thermal sensitivity of 1.11% K^{-1} and a minimum temperature uncertainty of 0.44 K, both recorded at room temperature. These nanodiscs were also investigated to be used as primary luminescent thermometers. However, the important amount of heat generated by the non-radiative relaxation processes to populate the $^2H_{11/2}$ and the $^4S_{3/2}$ energy levels of Er^{3+} from which the green emissions in which the luminescent thermometer is based, derived from the four-photon UC mechanism determined, invalidate the possibility of using these materials as potential primary luminescent thermometers.

V. Acknowledgments

This work was supported by the Spanish Government under projects MAT2016-75716-C2-1-R (AEI/FEDER, UE) and TEC2014-55948-R, and by the Generalitat de Catalunya under project 2017SGR755. A.N acknowledges financial support from the Generalitat de Catalunya under grant 2017FI_B00620, 2018FI_B100161 and 2019FI_B200154.

VI. References

[1] A. Nexha, J.J. Carvajal, M.C. Pujol, F. Díaz, M. Aguiló, Lanthanide doped luminescence nanothermometers in the biological windows: strategies and applications, Nanoscale 13 (2021) 7913-7987.

[2] L.R. Hirsch, R.J. Stafford, J.A. Bankson, S.R. Sershen, B. Rivera, R.E. Price, J.D. Hazle, N.J. Halas, J.L. West, Nanoshell-mediated near-infrared thermal therapy of tumors under magnetic resonance guidance, Proc. Natl. Acad. Sci. 100 (2003) 13549.

[3] C. Gota, K. Okabe, T. Funatsu, Y. Harada, S. Uchiyama, Hydrophilic fluorescent nanogel thermometer for intracellular thermometry, J. Am. Chem. Soc. 131 (2009) 2766-2767.

[4] K. Okabe, N. Inada, C. Gota, Y. Harada, T. Funatsu, S. Uchiyama, Intracellular temperature mapping with a fluorescent polymeric thermometer and fluorescence lifetime imaging microscopy, Nat. Commun. 3 (2012) 705.

[5] J.S. Donner, S.A. Thompson, M.P. Kreuzer, G. Baffou, R. Quidant, Mapping intracellular temperature using green fluorescent protein, Nano Lett. 12 (2012) 2107-2111.

[6] D. Ross, M. Gaitan, L.E. Locascio, Temperature measurement in microfluidic systems using a temperature-dependent fluorescent dye, Anal. Chem. 73 (2001) 4117-4123.

[7] S. Li, K. Zhang, J. M. Yang, L. Lin, H. Yang, Single quantum dots as local temperature markers, Nano Lett. 7 (2007) 3102-3105.

[8] M. Back, E. Trave, J. Ueda, S. Tanabe, Ratiometric optical thermometer based on dual near-infrared emission in Cr^{3+}-doped bismuth-based gallate host, Chem. Mater. 28 (2016) 8347-8356.

[9] G. Chen, H. Qiu, P.N. Prasad, X. Chen, Upconversion nanoparticles: design, nanochemistry, and applications in theranostics, Chem. Rev. 114 (2014) 5161-5214.

[10] A. Nexha, J.J. Carvajal, M.C. Pujol, F. Díaz, M. Aguiló, Synthesis of monoclinic Ho,Tm:KLu$(WO_4)_2$ microrods with high photothermal conversion efficiency via a thermal decomposition-assisted method, J. Mater. Chem. C 9 (2021) 2024-2036.

[11] D.K. Chatterjee, A.J. Rufaihah, Y. Zhang, Upconversion fluorescence imaging of cells and small animals using lanthanide doped nanocrystals, Biomaterials 29 (2008) 937-943.

[12] S.F. Lim, R. Riehn, W.S. Ryu, N. Khanarian, C. Tung, D. Tank, R.H. Austin, In vivo and scanning electron microscopy imaging of upconverting nanophosphors in *Caenorhabditis Elegans*, Nano Lett. 6 (2006) 169-174.

[13] S. Wilhelm, Perspectives for upconverting nanoparticles, ACS Nano 11 (2017) 10644-10653.

[14] L.H. Fischer, G.S. Harms, O.S. Wolfbeis, Upconverting nanoparticles for nanoscale thermometry, Angew. Chem., Int. Ed. 50 (2011) 4546-4551.

[15] A. Nexha, M.C. Pujol, J.J. Carvajal, F. Díaz, M. Aguiló, Effect of the size and shape of Ho, Tm:KLu$(WO_4)_2$ nanoparticles on their self-assessed photothermal properties, Nanomaterials, 11 (2021) 485.

[16] N.M. Bhiri, M. Dammak, M. Aguiló, F. Díaz, J.J. Carvajal, M.C. Pujol, Stokes and anti-Stokes operating conditions dependent luminescence thermometric performance of Er^{3+}-doped and Er^{3+}, Yb^{3+} co-doped $GdVO_4$ microparticles in the non-saturation regime, J. Alloys Compd. 814 (2020) 152197.

[17] X. Wang, X. Kong, Y. Yu, Y. Sun, H. Zhang, Effect of annealing on upconversion luminescence of ZnO:Er^{3+} nanocrystals and high thermal sensitivity, J. Phys. Chem. C, 111 (2007) 15119-15124.

[18] F. Wang, J. Wang, X. Liu, Direct evidence of a surface quenching effect on size-dependent luminescence of upconversion nanoparticles, Angew. Chem. Int. Ed. 122 (2010) 7618-7622.

[19] F. Vetrone, J. C. Boyer, J.A. Capobianco, A. Speghini, M. Bettinelli, Concentration-dependent near-infrared to visible upconversion in nanocrystalline and bulk Y_2O_3:Er^{3+}, Chem. Mater. 15 (2003) 2737-2743.

[20] J.A. Capobianco, F. Vetrone, J.C. Boyer, A. Speghini, M. Bettinelli, Enhancement of red emission ($^4F_{9/2}\rightarrow{}^4I_{15/2}$) via upconversion in bulk and nanocrystalline cubic Y_2O_3:Er^{3+}, J. Phys. Chem. B, 106 (2002) 1181-1187.

[21] M. Suta, A. Meijerink, A theoretical framework for ratiometric single ion luminescent thermometers-thermodynamic and kinetic guidelines for optimized performance, Adv. Theory Simul. 3 (2020) 2000176.

[22] F. Artizzu, F. Quochi, L. Marchiò, E. Sessini, M. Saba, A. Serpe, A. Mura, M.L. Mercuri, G. Bongiovanni, P. Deplano, Fully efficient direct Yb-to-Er energy transfer at molecular level in a near-infrared emitting heterometallic trinuclear quinolinolato complex, J. Phys. Chem. Lett. 4 (2013) 3062-3066.

[23] J.F. Philipps, T. Töpfer, H. Ebendorff-Heidepriem, D. Ehrt, R. Sauerbrey, Energy transfer and upconversion in erbium-ytterbium-doped fluoride phosphate glasses, Appl. Phys. B 74 (2002) 233-236.

[24] J. Silver, M.I. Martinez-Rubio, T.G. Ireland, G.R. Fern, R. Withnall, The effect of particle morphology and crystallite size on the upconversion luminescence properties of erbium and ytterbium co-doped yttrium oxide phosphors, J. Phys. Chem. B 105 (2001) 948-953.

[25] G. Liu, L. Fu, Z. Gao, X. Yang, Z. Fu, Z. Wang, Y. Yang, Investigation into the temperature sensing behavior of Yb3+ sensitized Er^{3+} doped Y_2O_3, YAG and $LaAlO_3$ phosphors, RSC Adv. 5 (2015) 51820-51827.

[26] O.A. Savchuk, P. Haro-González, J.J. Carvajal, D. Jaque, J. Massons, M. Aguiló, F. Díaz, Er:Yb:NaY_2F_5O up-converting nanoparticles for sub-tissue fluorescence lifetime thermal sensing, Nanoscale 6 (2014) 9727-9733.

[27] M. Haase, H. Schäfer, Upconverting nanoparticles, Angew. Chem. Int. Ed. 50 (2011) 5808-5829.

[28] A. Andreeva, A. Sisonyuk, E. Himich, Growth conditions, optical and dielectric properties of yttrium oxide thin films, Phys. Status Solidi A 145 (1994) 441-446.

[29] J. Petry, R. Komban, C. Gimmler, H. Weller, Simple one pot synthesis of luminescent europium doped yttrium oxide Y_2O_3:Eu nanodiscs for phosphor converted warm white LEDs, Nanoscale Adv. 4 (2022) 858-864.

[30] X. Jing, T.G. Ireland, C. Gibbons, D.J. Barber, J. Silver, A. Vecht, G. Fern, P. Trowga, D. Morton, Control of Y_2O_3:Eu spherical particle phosphor size, assembly properties, and performance for FED and HDTV, J. Electrochem. Soc. 146 (1999) 4654-4658.

[31] W. Wang, P. Zhu, Red photoluminescent Eu^{3+}-doped Y_2O_3 nanospheres for LED-phosphor applications: synthesis and characterization, Opt. Exp. 26 (2018) 34820-34829.

[32] R.D. Shannon, Revised effective ionic radii and systematic studies of interatomic distances in halides and chalcogenides, Acta Crystallogr. A 32 (1976) 751-767.

[33] Y.C. Kang, D.J. Seo, S.B. Park, H.D. Park, Morphological and optical characteristics of Y_2O_3:Eu phosphor particles prepared by flame spray pyrolysis, Jpn. J. Appl. Phys. 40 (2001) 4083.

[34] A. Camenzind, R. Strobel, F. Krumeich, S.E. Pratsinis, Luminescence and crystallinity of flame-made Y_2O_3:Eu^{3+} nanoparticles, Adv. Powder Technol. 8 (2007) 5-22.

[35] H. Wang, M. Uehara, H. Nakamura, M. Miyazaki, H. Maeda, Synthesis of well-dispersed Y_2O_3:Eu nanocrystals and self-assembled nanodisks using a simple non-hydrolytic route, Adv. Mater. 17 (2005) 2506-2509.

[36] R. Si, Y.W. Zhang, H.P. Zhou, L.D. Sun, C.H. Yan, Controlled-synthesis, self-assembly behavior, and surface-dependent optical properties of high-quality rare-earth oxide nanocrystals, Chem. Mater. 19 (2007) 18-27.

[37] S. Yin, M. Shinozaki, T. Sato, Synthesis and characterization of wire-like and near-spherical Eu_2O_3-doped Y_2O_3 phosphors by solvothermal reaction, J. Lumin. 126 (2007) 427-433.

[38] S. Zeng, K. Tang, T. Li, Z. Liang, 3D flower-like Y_2O_3:Eu^{3+} nanostructures:template-free synthesis and its luminescence properties, J. Colloid Interface Sci. 316 (2007) 921-929.

[39] A. Camenzind, R. Strobel, S.E. Pratsinis, Cubic or monoclinic Y_2O_3:Eu^{3+} nanoparticles by one step flame spray pyrolysis, Chem. Phys. Lett. 415 (2005) 193-197.

[40] Z. Qi, C. Shi, W. Zhang, W. Zhang, T. Hu, Local structure and luminescence of nanocrystalline Y_2O_3:Eu, Appl. Phys. Lett. 81 (2002) 2857-2859.

[41] T. Igarashi, M. Ihara, T. Kusunoki, K. Ohno, T. Isobe, M. Senna, Relationship between optical properties and crystallinity of nanometer Y_2O_3:Eu phosphor, Appl. Phys. Lett. 76 (2000) 1549-1551.

[42] A. Konrad, T. Fries, A. Gahn, F. Kummer, U. Herr, R. Tidecks, K. Samwer, Chemical vapor synthesis and luminescence properties of nanocrystalline cubic Y_2O_3:Eu, J. Lumin. 86 (1999) 3129-3133.

[43] M. Kottaisamy, D. Jeyakumar, R. Jagannathan, M. Mohan Rao, Yttrium oxide:Eu^{3+} red phosphor by self-propagating high temperature synthesis, Mater. Res. Bull. 31 (1996) 1013-1020.

[44] G.K. Das, T.T.Y. Tan, Rare-earth-doped and codoped Y_2O_3 nanomaterials as potential bioimaging probes, J. Phys. Chem. C 112 (2008) 11211-11217.

[45] S. Balabhadra, M.L. Debasu, C.D.S. Brites, R.A.S. Ferreira, L.D. Carlos, Upconverting nanoparticles working as primary thermometers in different media, J. Phys. Chem. C 121 (2017) 13962-13968.

[46] A. Nexha, M. C. Pujol, J. J. Carvajal, F. Díaz, M. Aguiló, Controlling the growth of colloidal rare earth oxides via wet chemical methodologies, To be submitted at Crystal Growth and Design (2022).

[47] J. Jeong, N. Kim, M. G. Kim, W. Kim, Generic synthetic route to monodisperse sub-10 nm lanthanide oxide nanodisks: a Modified digestive ripening process, Chem. Mater. 28 (2016) 172-179.

[48] R.A. Harris, P.M. Shumbula, H. van der Walt, Analysis of the interaction of surfactants oleic acid and oleylamine with iron oxide nanoparticles through molecular mechanics modeling, Langmuir 31 (2015) 3934-3943.

[49] D. den Engelsen, G.R. Fern, T.G. Ireland, D. Hudry, A.M.M. Abeykoon, D. Nykypanchuk, J.H. Dickerson, J. Silver, Ultrathin Y_2O_3:Eu^{3+} nanodiscs: spectroscopic investigations and evidence for reduced concentration quenching, Nanotechnology, 29 (2018) 455703.

[50] D. Chen, Y. Wang, Impurity doping: a novel strategy for controllable synthesis of functional lanthanide nanomaterials, Nanoscale 5 (2013) 4621-4637.

[51] D. Wang, Y. Kang, X. Ye, C.B. Murray, Mineralizer-assisted shape-control of rare earth oxide nanoplates, Chem. Mater. 26 (2014) 6328-6332.

[52] M. Klokkenburg, J. Hilhorst, B.H. Erné, Surface analysis of magnetite nanoparticles in cyclohexane solutions of oleic acid and oleylamine, Vib. Spectrosc. 43 (2007) 243-248.

[53] G.B. Deacon, R.J. Phillips, Relationships between the carbon-oxygen stretching frequencies of carboxylato complexes and the type of carboxylate coordination, Coord. Chem. Rev. 33 (1980) 227-250.

[54] E.W. Barrera, M.C. Pujol, F. Diaz, S.B. Choi, F. Rotermund, K.H. Park, M.S. Jeong, C. Cascales, Emission properties of hydrothermal Yb(3+), Er(3+) and Yb(3+), Tm(3+)-codoped Lu_2O_3 nanorods: upconversion, cathodoluminescence and assessment of waveguide behavior, Nanotechnology 22 (2011) 075205.

[55] M. Pollnau, D.R. Gamelin, S.R. Lüthi, H.U. Güdel, M.P. Hehlen, Power dependence of upconversion luminescence in lanthanide and transition-metal-ion systems, Phys. Rev. B 61 (2000) 3337-3346.

[56] F. Vetrone, R. Naccache, V. Mahalingam, C.G. Morgan, J.A. Capobianco, The active-core/active-shell approach: a strategy to enhance the upconversion luminescence in lanthanide-doped nanoparticles, Adv. Funct. Mater. 19 (2009) 2924-2929.

[57] Y. P. Peng, W. Lu, P. Ren, Y. Ni, Y. Wang, P. Yan, Y. J. Zeng, W. Zhang, S. Ruan, Multi-band up-converted lasing behavior in $NaYF_4$:Yb/Er nanocrystals, Nanomaterials, 8 (2018) 497.

[58] G.Y. Chen, Y. Liu, Z.G. Zhang, B. Aghahadi, G. Somesfalean, Q. Sun, F.P. Wang, Four-photon upconversion induced by infrared diode laser excitation in rare-earth-ion-doped Y_2O_3 nanocrystals, Chem. Phys. Lett. 448 (2007) 127-131.

[59] H. Huang, M. Yuan, S. Hu, Y. Zhong, W. Cui, C. Guo, C. Song, G. Zhao, K. Han, Nanosecond kinetics of multiphoton upconversion in an optically trapped single microcrystal, J. Mater. Chem. C 10 (2022) 9208-9215.

[60] C.D.S. Brites, A. Millán, L.D. Carlos, Chapter 281 - Lanthanides in Luminescent Thermometry, in: B. Jean-Claude, P. Vitalij K (Eds.) Handbook on the Physics and Chemistry of Rare Earths, Elsevier, 2016, pp. 339-427.

[61] R. Ao, L. Xing, W. Yang, A high-brightness phosphor based on Yb^{3+}/Er^{3+} codoped Y_2O_3 micro-crystals and controllable temperature sensing sensitivity via rare earth ions, Opt. Commun. 492 (2021) 126967.

[62] M. Quintanilla, E. Cantelar, F. Cussó, M. Villegas, A.C. Caballero, Temperature sensing with up-converting submicron-sized $LiNbO_3$:Er^{3+}/Yb^{3+} particles, Appl. Phys. Exp. 4 (2011) 022601.

[63] M. Mondal, V.K. Rai, C. Srivastava, Influence of silica surface coating on optical properties of Er^{3+}-Yb^{3+}:$YMoO_4$ upconverting nanoparticles, Chem. Eng. J. 327 (2017) 838-848.

[64] H. Lu, H. Hao, Y. Gao, G. Shi, Q. Fan, Y. Song, Y. Wang, X. Zhang, Dual functions of Er^{3+}/Yb^{3+} codoped $Gd_2(MoO_4)_3$ phosphor: temperature sensor and optical heater, J. Lumin. 191 (2017) 13-17.

[65] A. Siaï, P. Haro-González, K. Horchani Naifer, M. Férid, Optical temperature sensing of Er^{3+}/Yb^{3+} doped $LaGdO_3$ based on fluorescence intensity ratio and lifetime thermometry, Opt. Mater. 76 (2018) 34-41.

[66] S. Du, X. Ma, Q. Qiang, G. Zhang, Y. Wang, Emission in $Gd_6O_5F_8$:Yb^{3+},Er^{3+} micro-particles for multimodal luminescence and temperature sensing upon 980 nm excitation, Phys. Chem. Chem. Phys. 18 (2016) 26894-26899.

[67] G. Xiang, X. Liu, J. Zhang, Z. Liu, W. Liu, Y. Ma, S. Jiang, X. Tang, X. Zhou, L. Li, Y. Jin, Dual-mode optical thermometry based on the fluorescence intensity ratio excited by a 915 nm wavelength in $LuVO_4$:Yb^{3+}/Er^{3+}@SiO_2 nanoparticles, Inorg. Chem. 58 (2019) 8245-8252.

[68] B. Dong, D.P. Liu, X.J. Wang, T. Yang, S.M. Miao, C.R. Li, Optical thermometry through infrared excited green upconversion emissions in Er^{3+}-Yb^{3+} codoped Al_2O_3, Appl. Phys. Lett. 90 (2007) 181117.

[69] L. Xu, J. Liu, L. Pei, Y. Xu, Z. Xia, Enhanced up-conversion luminescence and optical temperature sensing in graphitic C3N4 quantum dots grafted with $BaWO_4$:Yb^{3+},Er^{3+} phosphors, J. Mater. Chem. C 7 (2019) 6112-6119.

[70] X. Yang, Z. Wu, Z. Yang, X. Zhao, C. Song, M. Yuan, K. Han, H. Wang, S. Li, X. Xu, Flame-made Y_2O_3:Yb^{3+}/Er^{3+} upconversion nanoparticles: mass production synthesis, multicolor tuning and thermal sensing studies, J. Alloys Compd. 854 (2021) 157078.

[71] A.K. Soni, A. Kumari, V.K. Rai, Optical investigation in shuttle like $BaMoO_4:Er^{3+}$-Yb^{3+} phosphor in display and temperature sensing, Sens. Actuators B Chem. 216 (2015) 64-71.

[72] R.G. Geitenbeek, P.T. Prins, W. Albrecht, A. van Blaaderen, B.M. Weckhuysen, A. Meijerink, $NaYF_4:Er^{3+},Yb^{3+}/SiO_2$ core/shell upconverting nanocrystals for luminescence thermometry up to 900 K, J. Phys. Chem. C 121 (2017) 3503-3510.

[73] S.P. Tiwari, M.K. Mahata, K. Kumar, V.K. Rai, Enhanced temperature sensing response of upconversion luminescence in $ZnO\text{-}CaTiO_3:Er^{3+}/Yb^{3+}$ nano-composite phosphor, Spectrochim. Acta A Mol. Biomol. Spectrosc. 150 (2015) 623-630.

[74] A. Pandey, V.K. Rai, V. Kumar, V. Kumar, H.C. Swart, Upconversion based temperature sensing ability of Er^{3+}-Yb^{3+} codoped $SrWO_4$: an optical heating phosphor, Sens. Actuators B Chem. 209 (2015) 352-358.

[75] O.A. Savchuk, J.J. Carvajal, C. Cascales, M. Aguiló, F. Díaz, Benefits of silica core-shell structures on the temperature sensing properties of Er, Yb:$GdVO_4$ up-conversion nanoparticles, ACS Appl. Mater. Interfaces 8 (2016) 7266-7273.

[76] R. Dey, V.K. Rai, Yb^{3+} sensitized Er^{3+} doped La_2O_3 phosphor in temperature sensors and display devices, Dalt. Trans. 43 (2014) 111-118.

[77] M.K. Mahata, K. Kumar, V.K. Rai, Er^{3+}-Yb^{3+} doped vanadate nanocrystals: a highly sensitive thermographic phosphor and its optical nanoheater behavior, Sens. Actuators B Chem. 209 (2015) 775-780.

[78] S. Singh, K. Kumar, S.B. Rai, Er^{3+}/Yb^{3+} codoped Gd_2O_3 nano-phosphor for optical thermometry, Sens. Actuators A Phys. 149 (2009) 16-20.

[79] M. Lin, L. Xie, Z. Wang, B.S. Richards, G. Gao, J. Zhong, Facile synthesis of mono-disperse sub-20 nm $NaY(WO_4)_2:Er^{3+},Yb^{3+}$ upconversion nanoparticles: a new choice for nanothermometry, J. Mater. Chem. C, 7 (2019) 2971-2977.

[80] Y. Liu, G. Bai, E. Pan, Y. Hua, L. Chen, S. Xu, Upconversion fluorescence property of Er^{3+}/Yb^{3+} codoped lanthanum titanate microcrystals for optical thermometry, J. Alloys Compd. 822 (2020) 153449.

[81] R.G. Geitenbeek, B.B.V. Salzmann, A. E. Nieuwelink, A. Meijerink, B.M. Weckhuysen, Chemically and thermally stable lanthanide-doped Y_2O_3 nanoparticles for remote temperature sensing in catalytic environments, Chem. Eng. Sci. 198 (2019) 235-240.

[82] N. Rakov, G.S. Maciel, Three-photon upconversion and optical thermometry characterization of Er^{3+}:Yb^{3+} co-doped yttrium silicate powders, Sens. Actuators B Chem. 164 (2012) 96-100.

[83] A. Ćirić, T. Gavrilović, M.D. Dramićanin, Luminescence intensity ratio thermometry with Er^{3+}: performance overview, Crystals 11 (2021) 189-208.

[84] S.F. León-Luis, U.R. Rodríguez-Mendoza, E. Lalla, V.J.S. Lavín, A.B. Chemical, Temperature sensor based on the Er^{3+} green upconverted emission in a fluorotellurite glass, Sens. Actuators B Chem. 158 (2011) 208-213.

[85] E.E. Brown, U. Hömmerich, A. Bluiett, C. Kucera, J. Ballato, S. Trivedi, Near-infrared and upconversion luminescence in Er:Y_2O_3 ceramics under 1.5 μm excitation, J. Am. Ceram. Soc. 97 (2014) 2105-2110.